



Thermoelectric analysis of $(\text{Bi}_{0.98}\text{In}_{0.02})_2\text{Te}_{2.7}\text{Se}_{0.3}$ /polyaniline and $(\text{Bi}_{0.98}\text{In}_{0.02})_2\text{Se}_{2.7}\text{Te}_{0.3}$ /polyaniline composites

Ganesh Shridhar Hegde^{1,2}, A. N. Prabhu^{2,*} , Suchitra Putran², Megha Y. Bhat², and P. D. Babu³

¹ Department of Physics, Post graduate Section, KLE's society S. Nijalingappa College, Rajaji nagara, Bengaluru 560010, India

² Department of Physics, Manipal Institute of Technology, Manipal Academy of Higher Education, Manipal 576104, India

³ UGC-DAE Consortium for Scientific Research, Mumbai Centre, Bhabha Atomic Research Centre, R-5 Shed, Trombay, Mumbai 400085, India

Received: 1 August 2023

Accepted: 14 September 2023

Published online:
30 September 2023

© The Author(s), 2023

ABSTRACT

The present study examines the thermoelectric (TE) properties of Polyaniline (PANI) in $(\text{Bi}_{0.98}\text{In}_{0.02})_2\text{Te}_{2.7}\text{Se}_{0.3}$ (BIT) and $(\text{Bi}_{0.98}\text{In}_{0.02})_2\text{Se}_{2.7}\text{Te}_{0.3}$ (BIS), compounds created using solid-state reaction in the temperature interval 10 to 350 K. The XRD study reveals hexagonal crystal structure with a space group of $R\bar{3}m$. The composite samples have grains that resemble hair like structure because size of the grains above the surfaces has expanded irregularly, and selenium has been shown to concentrate at the grain borders. Electrical resistivity in BIS/PANI has found decreased by 6 times compared to BIT/PANI. The decrease in overall thermal conductivity is strongly influenced by the interface scattering effect of PANI composites and the BIT/BIS grain boundaries. The thermal conductivity of pure BIT is found to decrease by 1.5 and 1.4 times, respectively, than that of BIT/PANI and BIS/PANI. In comparison to pure BIT and BIS samples, the ZT value of BIT/PANI has been raised by a factor of 20.

1 Introduction

Thermoelectric (TE) energy is an efficient, affordable, and renewable green energy source that reduces our dependence on nuclear and carbon-based fossil fuels. TE solid-state devices are small, simple to build, and require no maintenance, and can easily transfer the vast reservoirs of heat energy from solar, geothermal and automotive sources into electricity. TE figure of merit (ZT) can be used to represent material's

competency ($ZT = \frac{S^2T}{\kappa\rho}$) [1]. The Seebeck coefficient, electrical resistivity, thermal conductivity and operating temperature, respectively, are represented as S , ρ , K and T . The majority of long-term initiatives in the field of TE devices have been centred primarily on inorganic TE materials like chalcogenides-bismuth telluride (Bi_2Te_3), bismuth selenide (Bi_2Se_3), lead telluride (PbTe), tin telluride (SnTe), tin selenide (SnSe), copper telluride (Cu_7Te_4), copper selenide (Cu_{2-x}Se), PbTe-SrTe

Address correspondence to E-mail: ashwatha.prabhu@manipal.edu

E-mail Addresses: ganeshhegde358@gmail.com; suchitrasp@gmail.com; megha62665@gmail.com; pdbabu@barc.gov.in

doped with Na_2Te , alloys, conducting oxides, and other carbon nanofillers, and so on [2–9]. However, their wider applications have been constrained by expensive raw materials, high processing costs, heavy metal contamination and challenge of large-scale processing [10].

The ordering of the molecular structure has a significant impact on the electrical transport characteristics of composites made from PANI molecules. The charge carrier transport is anticipated to take place via the potent benzenoid-quinoid ring-to-ring contact. The tight coil shape and haphazard molecular organization of PANI are well known [11]. The higher degree of ordering in the chain packing modifies the hopping activation energy and hopping free path, which in turn affects carrier mobility and electrical conductivity. Due to the energetically more advantageous mixing of the band structures of $\text{Bi}_2\text{Te}_3/\text{Bi}_2\text{Se}_3$ and PANI's system, it may be assumed that PANI is currently growing along the surface of Bi_2Te_3 and Bi_2Se_3 [12].

Because of high electrical conductivity of PANI, it can be used as a composite material in this system. Being located at the grain boundaries, PANI enhances the phonon scattering when added to the $(\text{Bi}_{0.98}\text{In}_{0.02})_2\text{Te}_{2.7}\text{Se}_{0.3}$ and $(\text{Bi}_{0.98}\text{In}_{0.02})_2\text{Se}_{2.7}\text{Te}_{0.3}$ matrix. As a result, it is anticipated that the matrix diffusion during sintering will be inhibited, preserving the small grain size, and that the interface scattering phenomena would be used to control the carrier concentration. We anticipate a modification in the TE property because of $\text{Te}_{\text{Se}}/\text{Se}_{\text{Te}}$ combined effects on Bi_{In} antisite defects and PANI interfaces, which is the driving force for the current work [13].

Mohammad Noorozi et al. [14] have shown a physical model to characterize the TE materials of SiGe Nanowire in a back-gate arrangement. Biasing voltage to the gate at various temperatures altered the carrier transport in nanowires. Compared to bulk SiGe, the power factor of SiGe nanowires was found to increase by a factor of more than 2 in the temperature range 273 to 450 K. Micro-TE generators of SiGe (μTEG) are promising for energy supply by using daily waste heat. Si nanowire and SiGe nanowire are candidates due to their high electric conductivity and low thermal conductivity performance. The review by You et al. provides a comprehensive introduction to Si and SiGe nanowires, their basic TE principles, materials, structures, fabrication and measurements [15].

Since Bi_2Te_3 and Bi_2Se_3 alloys have the highest known TE efficiency at low and near room

temperatures, they constitute the most significant class of TE materials, while silicon-based alloys are typically employed in TE applications that need high temperatures (> 600 K). Recently, Bi_2Te_3 solid-state devices dominated the market for temperature control applications. As per the need to eliminate greenhouse-gas effect, Peltier cooling systems are attracting more attention especially in the portable systems because their efficiencies are comparable to traditional refrigerant-based coolants.

The composite of $(\text{Bi}_{0.98}\text{In}_{0.02})_2\text{Te}_{2.7}\text{Se}_{0.3}$ with reduced graphene oxide in varying quantities was discussed in our earlier study [16]. We were successful in enhancing the TE performance of $(\text{Bi}_{0.98}\text{In}_{0.02})_2\text{Se}_{2.7}\text{Te}_{0.3}$ at low to near room temperature. This work examines the TE performance in the temperature range 10 to 350 K and reports on a novel one-step preparation to include PANI in $(\text{Bi}_{0.98}\text{In}_{0.02})_2\text{Te}_{2.7}\text{Se}_{0.3}$ and $(\text{Bi}_{0.98}\text{In}_{0.02})_2\text{Se}_{2.7}\text{Te}_{0.3}$. Electrical resistivity in BIS/PANI was observed to be 6 times less than that in BIT/PANI. The novelty of the current study is that the ZT value of BIT/PANI is found to increase by a factor of 20 compared to pure BIT and BIS samples.

2 Synthesis and characterization technique

2.1 Synthesis of BIS, BIT, BIS/PANI and BIT/PANI composites

Polycrystalline samples of BIS and BIT were prepared using solid-state reaction method. To create a uniform mixture, the elements bismuth, tellurium, indium and selenium were combined in stoichiometric proportions and ground for two hours using an agate mortar and pestle. Under 5-ton hydraulic press compression, the powder was pelletized. The pellets were sealed in a quartz tube in an atmosphere of argon at a pressure of 10^{-3} Torr. After that, the sealed sample was sintered for 12 h at a temperature of around 150°C . After being sintered, the samples of BIS and BIT were ground for 1.5 h. Polyaniline (PANI) was stoichiometrically added to the resulting mixture, crushed for 30 min and pelletized with the dimension of $5 \times 2 \times 10\text{mm}^3$.

2.2 Characterization of synthesized composites

Powder X-ray diffraction study was carried out using $\text{Cu K}\alpha$ rays. Using X-ray diffractometer (Rigaku Miniflex), the compounds' purity, crystallinity and phase

formation were analysed. The “JEOL JSM-7100F” instrument was used to perform field emission scanning electron microscopy (FESEM) at the magnification of 35 kX and voltage of 15 kV. The “Physical Property Measurement System” (PPMS) was used to measure the temperature-dependent electrical resistivity, Seebeck coefficient, thermal conductivity and *ZT* values of the composites over the temperature range of 10 to 350 K.

3 Result and discussion

3.1 X-ray diffraction

Powder X-ray diffraction was performed between 20° and 80° degrees at a scan rate of 2 degrees per minute to determine the structure, purity and crystallinity of BIS/PANI and BIT/PANI and is shown in Fig. 1. XRD patterns of BIS/PANI and BIT/PANI depict hexagonal crystal structure with *R* 3 *m* space group and

all the samples exhibit (105) as most aligned XRD peak plane, confirming the absence of impurities. In BIT/PANI composite, the diffraction peaks are amorphous due to the presence of PANI, with a reduction in full width at half maximum (FWHM) that can be attributed to the ordered inter-chain stacking or molecular organisation of polymer chain [17]. The JCPDS data of Bi₂Te₃ and Bi₂Se₃ have been extracted from “Materials research project” and are in good agreement with the present obtained XRD patterns. Table 1 lists the average crystallite size calculated by Williamson–Hall for as-deposited and 0.02wt% PANI-doped samples. It has been observed that grain size reduces with increasing PANI to Bi₂Se₃ concentration. Similarly, there is a similar broadening and shifting of XRD peak (Fig. 2) patterns for BIT/PANI-doped sample at 28° compared to BIT. The dominant peak is detected at an angle of 28°, which demonstrates the mono distribution of periodicity of the repeat unit of the PANI and the ordering of the molecular organisation of the PANI in the Bi₂Te₃ and

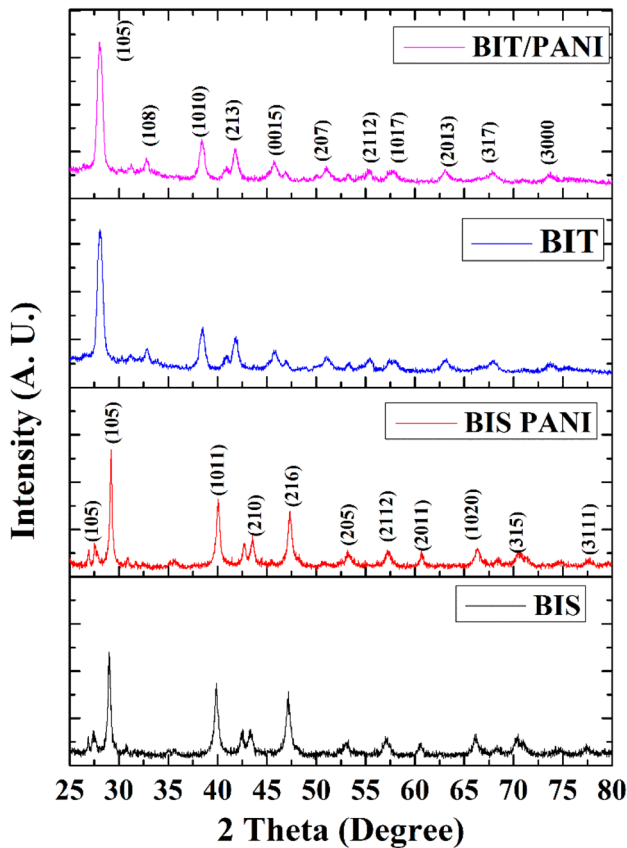


Fig. 1 X-ray diffraction pattern of BIT/PANI and BIS/PANI composites

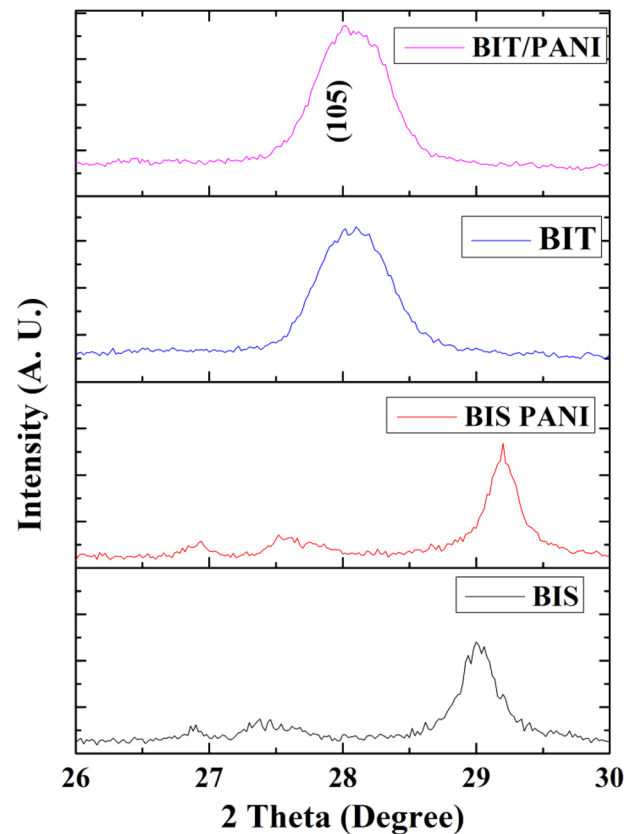


Fig. 2 Shifting of XRD pattern of BIT/PANI and BIS/PANI composites

Bi_2Se_3 matrix. Bi atoms are surrounded by Te/Se(1) and Te/Se(2) atoms on either side, while Te/Se(2) atoms are surrounded by Bi atoms on both sides. Each sandwich-like structure is created from the five-layer sequence [Te(1)-Bi-Te(2)-Bi-Te(1)] [18]. The weak van der Waals forces are primarily responsible for the link between the neighbouring Te/Se(1) layers (Fig. 3). When Bi_2Te_3 and aniline are present, BIT/BIS is encased in PANI, leading to an energetically more favourable mixing of the band structures of Bi_2Te_3 and Bi_2Se_3 at the Te(1)/Se(1) site of the weak van der Waals force and system [19]. To validate the XRD peak patterns, Rietveld refinement factors such as R_p ,

R_{wp} , R_{ep} and χ^2 have been found and are provided in Table 1 (Fig. 4).

3.2 Field emission scanning electron microscopy (FESEM) and energy dispersive X-ray analysis of spectra (EDS)

Figure 5 shows the surface morphological features of synthesized BIT/PANI and BIS/PANI polycrystalline samples. According to the FESEM investigation, as PANI is introduced to the molecule, it is seen that the pore size decreases [16]. It can infer from Fig. 5a and b, that decrease in porosity partially causes selenium volatilization. Due to the high vapour pressure,

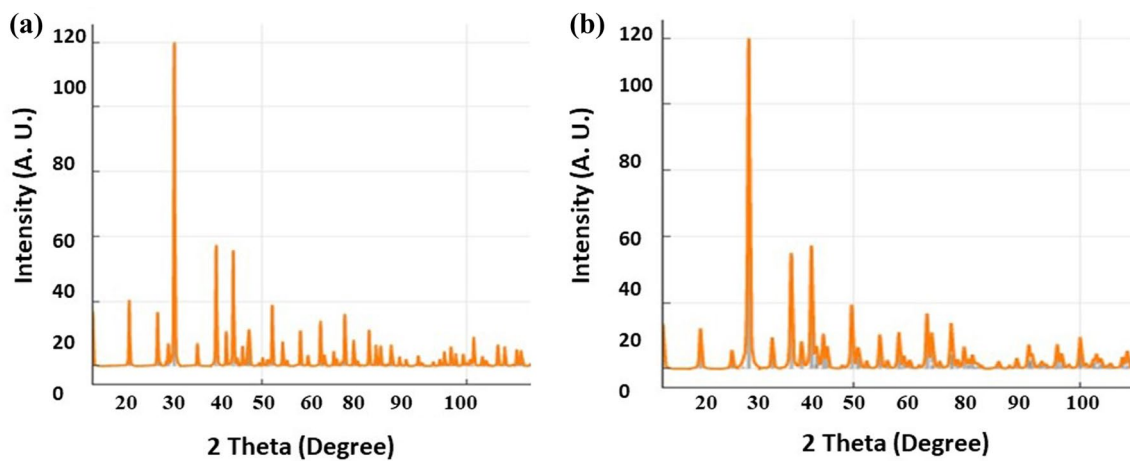


Fig. 3 a JCPDS Files of Bi_2Te_3 (Id: mp34302) and b Bi_2Se_3 (Id: mp541387) (Adapted from Materials research project)

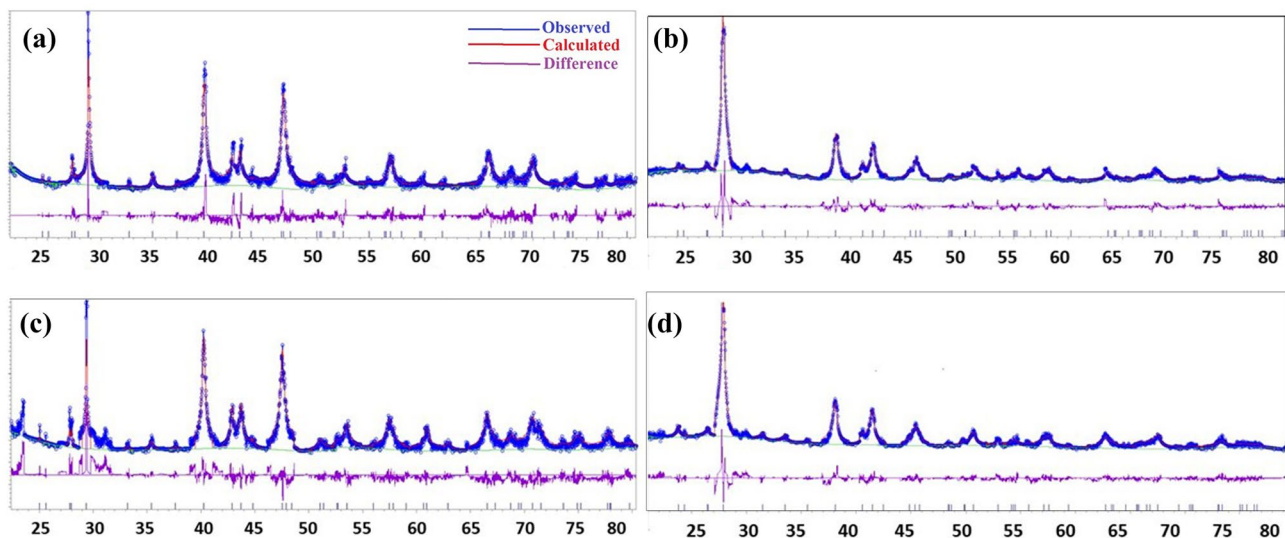
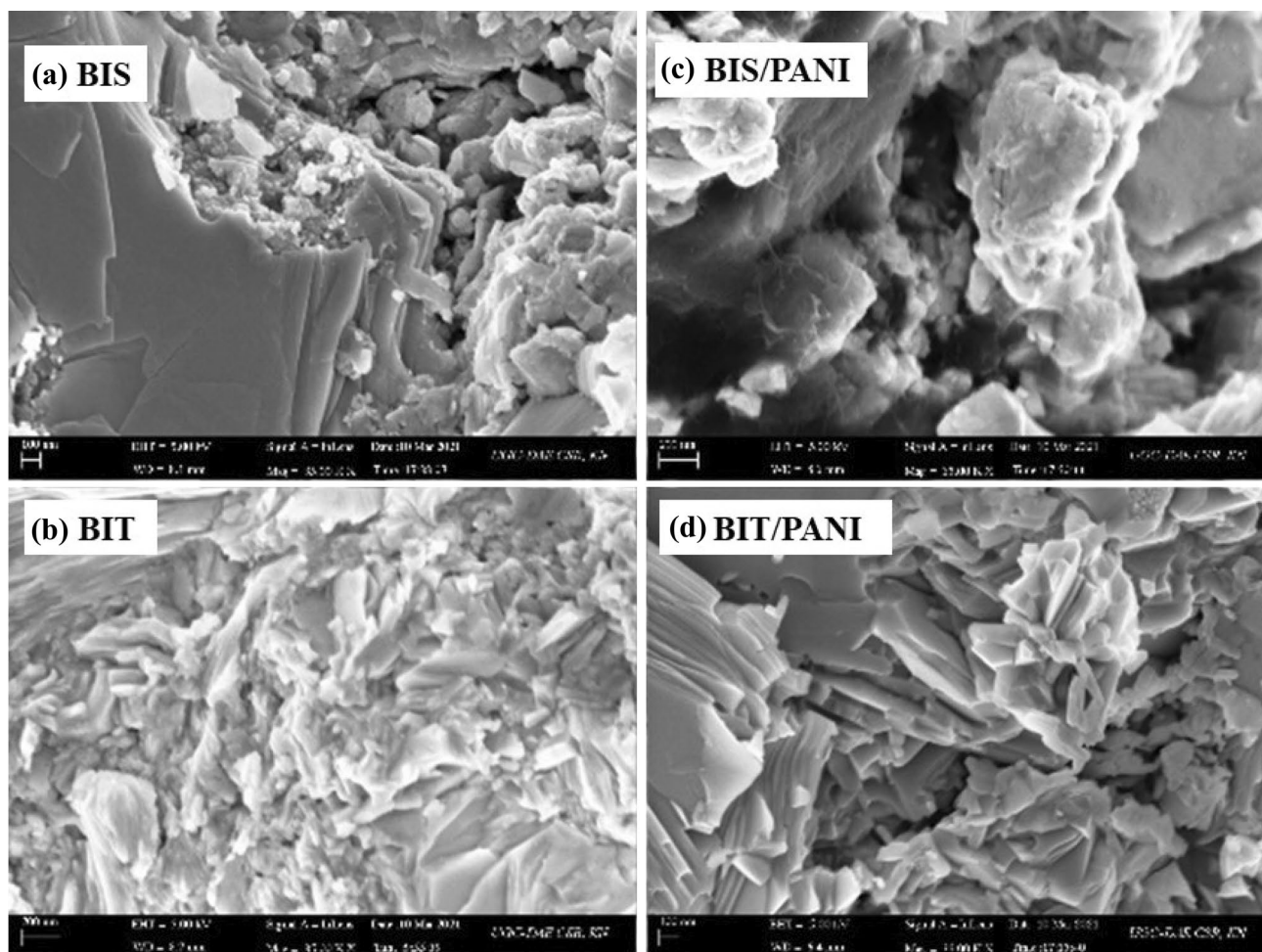


Fig. 4 Rietveld refinement images of BIT/PANI and BIS/PANI composites

Table 1 XRD analysis data of BIT/PANI and BIS/PANI composites

Sample	R_p	R_{wp}	R_{cp}	χ^2	crystallite size(nm)	$a = b$ Å ± 0.005	c Å ± 0.005	Lattice strain ± 0.0001
$(Bi_{0.98}In_{0.02})_2Te_{2.7}Se_{0.3}$	7.128	9.58	6.945	1.905	421.0	4.340	30.146	0.0070
$(Bi_{0.98}In_{0.02})_2Te_{2.7}Se_{0.3}/0.02wt\%$ Polyaniline	6.212	8.21	7.091	1.325	180.2	4.290	29.819	0.0031
$(Bi_{0.98}In_{0.02})_2Se_{2.7}Te_{0.3}$	12.83	16.46	13.14	1.674	37.40.7	4.1466	28.7165	0.0019
$(Bi_{0.98}In_{0.02})_2Se_{2.7}Te_{0.3}/0.02wt\%$ Polyaniline	11.15	14.79	11.30	1.711	64.10.6	4.1631	28.8384	0.0031

**Fig. 5** FESEM images of **a** BIS **b** BIT **c** BIS/PANI and **d** BIT/PANI composites

selenium found to volatilize in some locations [20]. A network distribution with considerable gaps between them is shown in Fig. 5b. The grain size above the surfaces has expanded irregularly due to severe Te_{se}/Se_{Te} voids, as seen in Fig. 5c. The PANI fibres that deposit at the grain boundaries in the composite samples give them the appearance of hair (Fig. 5b and d) [21].

To identify the components in the composites, an EDS investigation was conducted. While components like bismuth, tellurium, selenium and indium are found in the BIS and BIT composite, the BIS/PANI composite has oxygen as an extra element (Fig. 6). The surface of the compound, which is seen in EDS

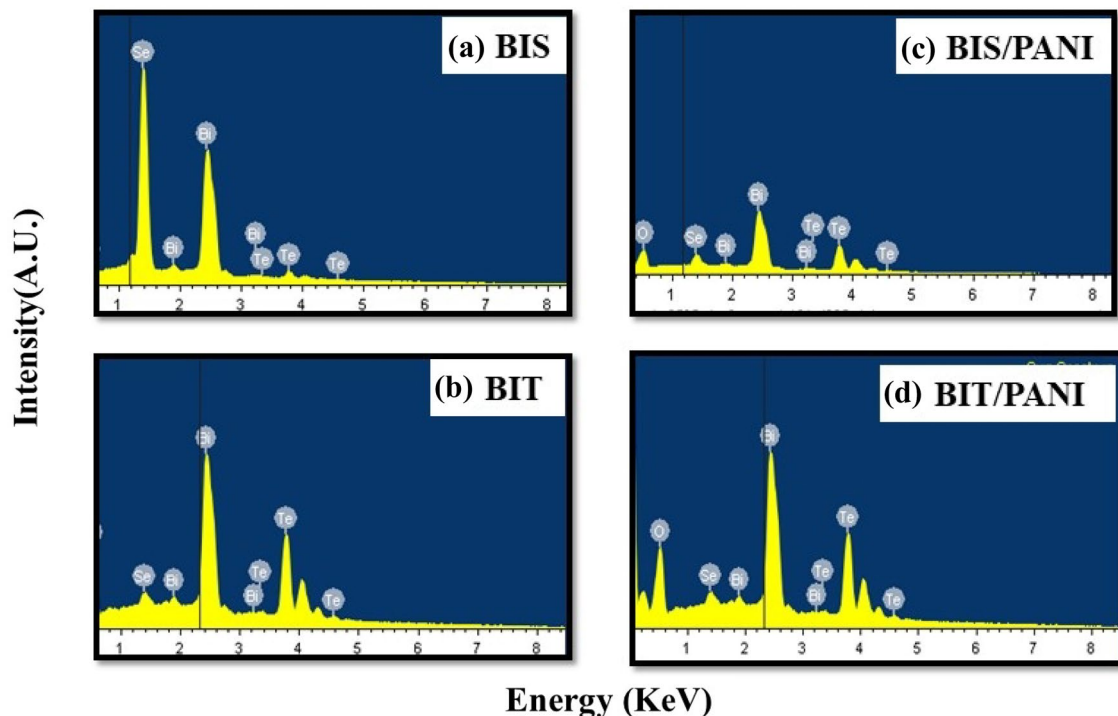


Fig. 6 EDS images of **a** BIS **b** BIT **c** BIS/PANI and **d** BIT/PANI composites

mapping of Fig. 7, is evenly distributed with each of the BIS, BIT, BIT/PANI and BIS/PANI components.

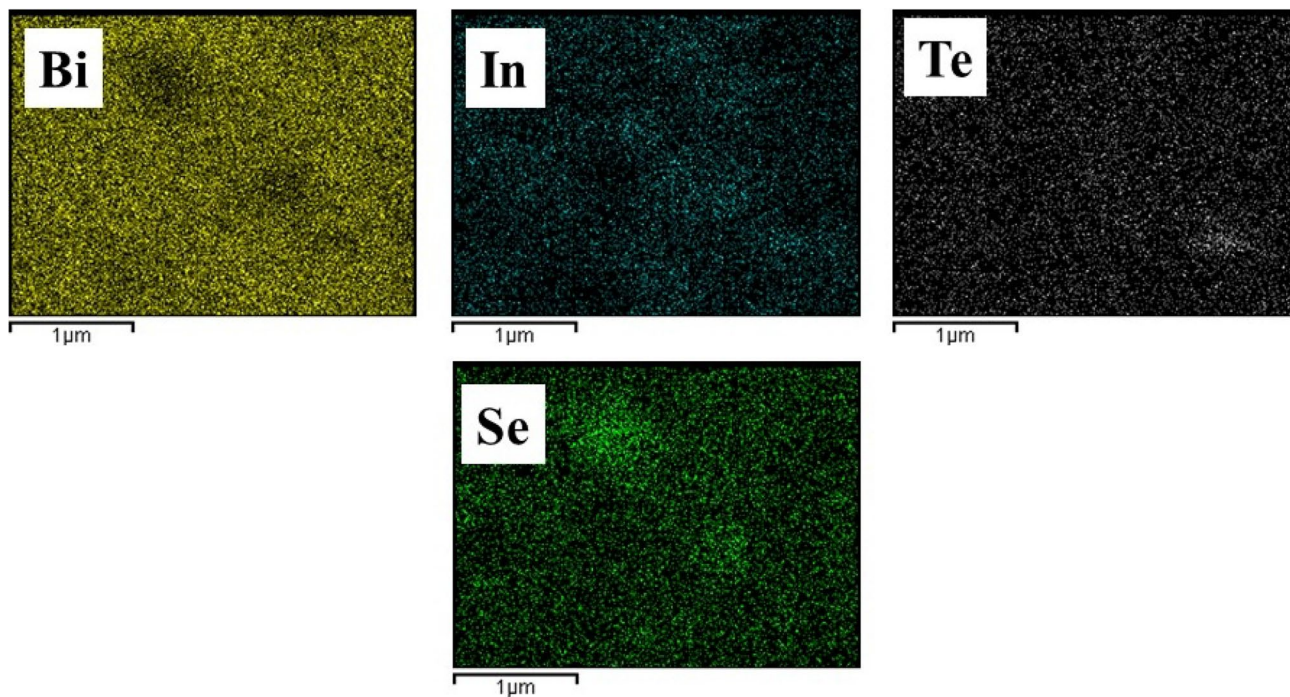
3.3 Electrical resistivity

Prepared BIT/PANI and BIS/PANI composites were tested for electrical resistivity in the temperature range 10–350 K (Fig. 8). During the entire temperature range, all of the samples exhibit *n*-type semiconducting behaviour. With increasing temperature, the electrical resistivity curve shows a sharp drop in value, confirming the material's semiconducting nature [22]. Charge transport in the conducting polymer PANI in Bi_2Te_3 and Bi_2Se_3 relates to metallic conduction within the metal islands via a hopping or tunnelling effect because of the insulating barriers [23]. As pure BIT and BIS possess more electrons than the corresponding BIT/PANI and BIS/PANI samples, their respective electrical resistivity curves show higher resistivity. As the PANI is providing an additional transmission route for the electrons, the carrier concentration rises [24]. By decreasing the double Schottky barrier band alignment between BIS and BIT, PANI facilitates the release of trapped electrons. Because of this arrangement, electrons may flow more freely, elevating the carrier concentration. Unfortunately, the PANI-generated

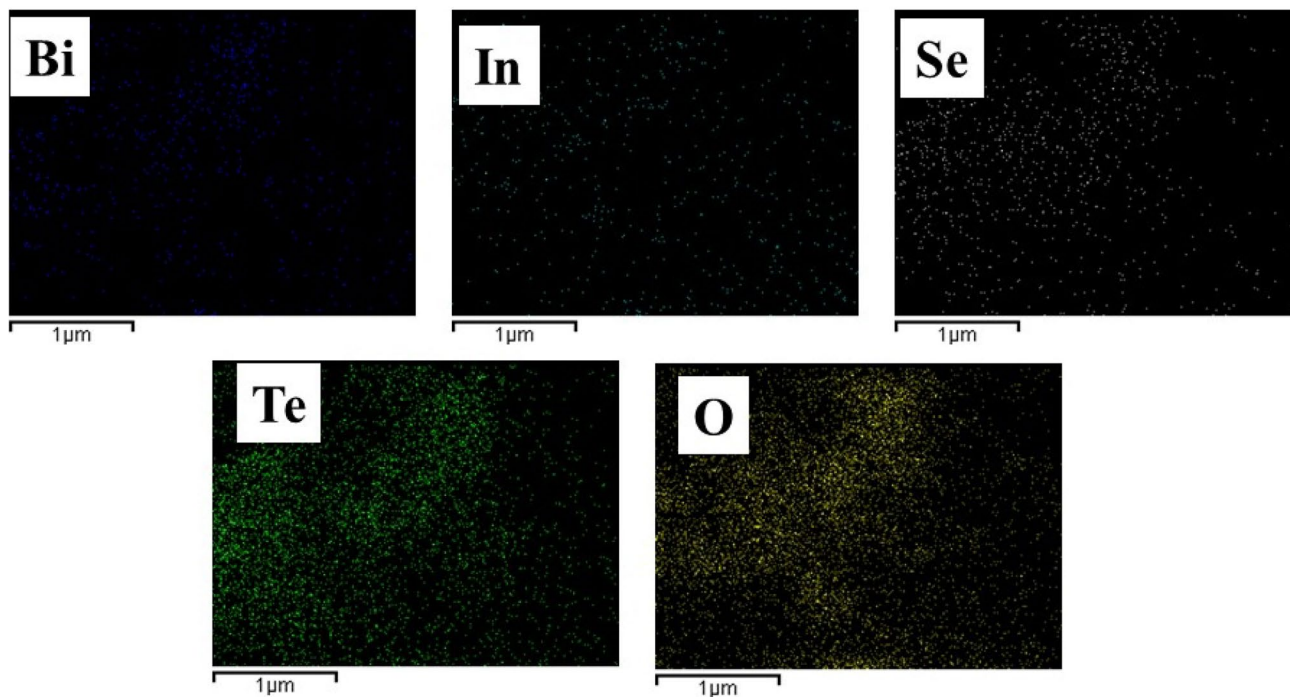
interfaces slow down the process because the interfaces show more charge dispersion. For PANI-based composites, the electrical transport characteristics are particularly sensitive to the molecular structure's degree of order [25]. It is hypothesised that charge carriers are transported via the strong contact between the benzenoid and quinoid rings. The molecular structure of PANI is well documented as a compact coil with a disordered molecular arrangement.

The energy barriers present between BIT, BIS and PANI prevent conducting electrons from moving across the grain boundaries easily. On the crystal surface, selenium partly segregates, resulting in the formation of positively charged selenium vacancies $V_{(\text{Se})}$ whose charge is balanced by free electrons [26]. The migration of selenium into the layers of tellurium dominates the free electron concentration. The degeneracy of the compounds is caused by the minimal interaction of PANI with BIT and BIS. As a result, the development of distinct energy levels leads to an increase in the electron concentration in the conduction band [27].

Between 115 and 250 K, the small polaron hopping model (SPH) is used (Fig. 9). Here, the activation energy (*EA*) is calculated using the slope of the linear fit. It has been noticed that polaron hopping,

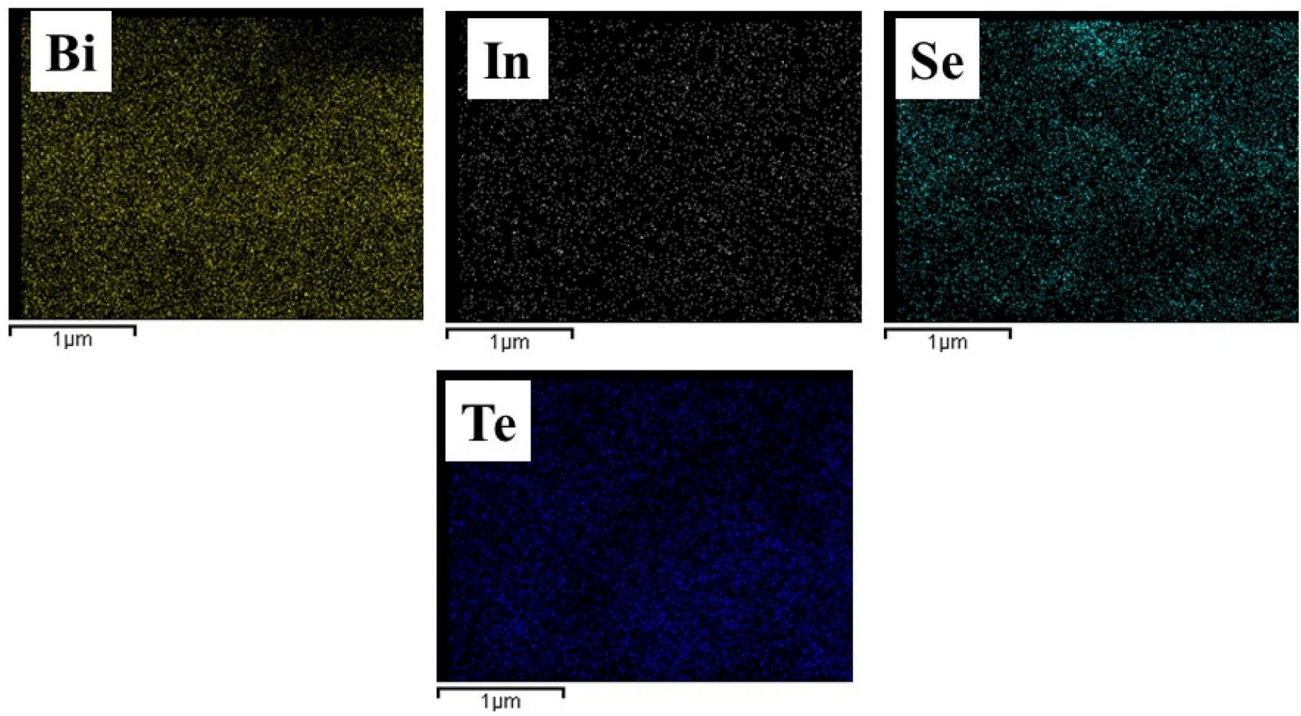


(a) BIS

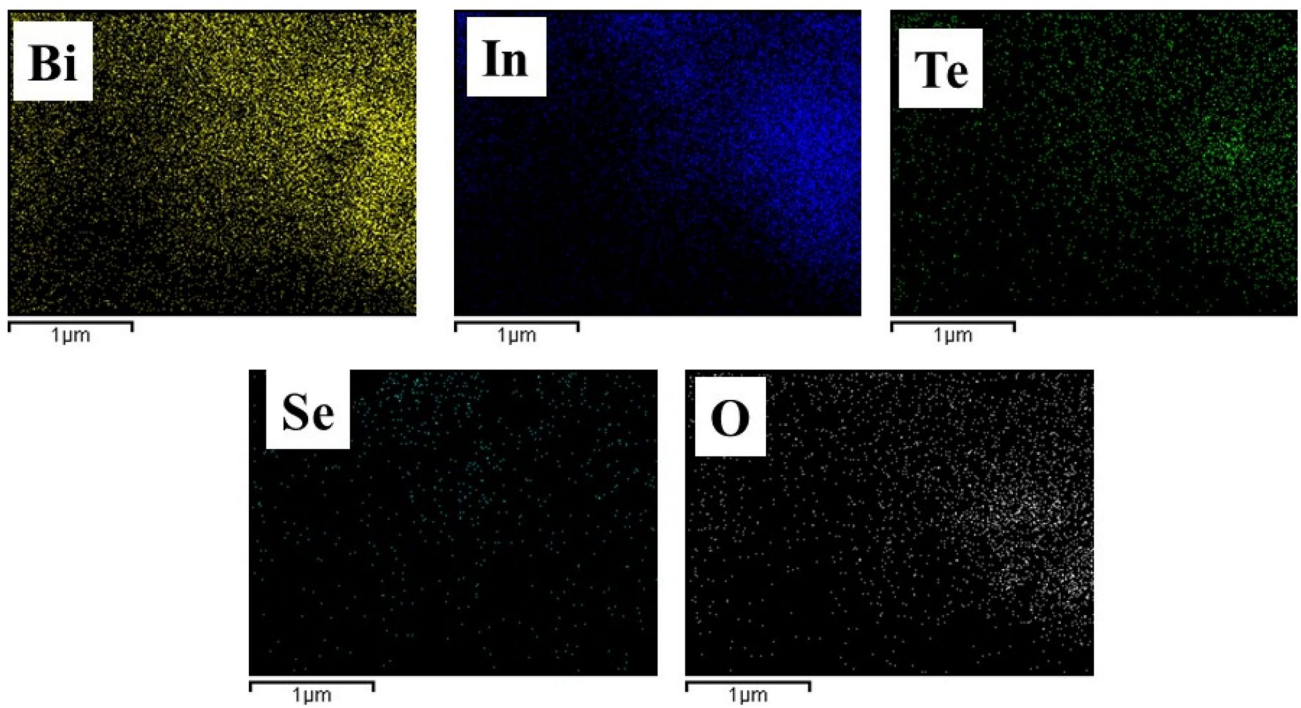


(b) BIS/PANI

Fig. 7 EDS mapping of **a** BIS **b** BIS/PANI **c** BIT **d** BIT/PANI composites



(c) BIT



(d) BIT/PANI

Fig. 7 continued

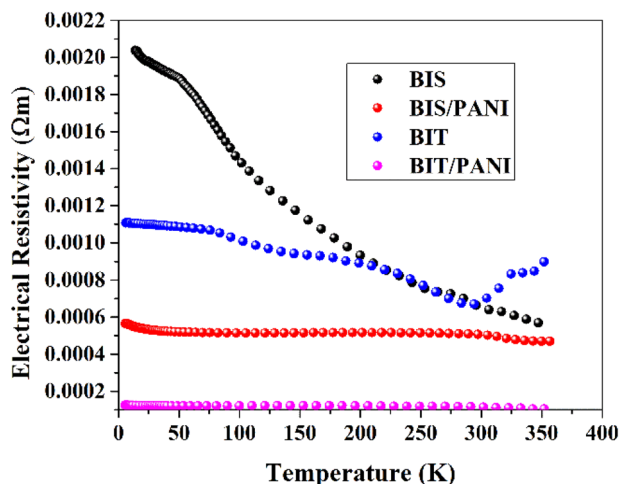


Fig. 8 Temperature-dependent electrical resistivity of BIT/PANI and BIS/PANI composites

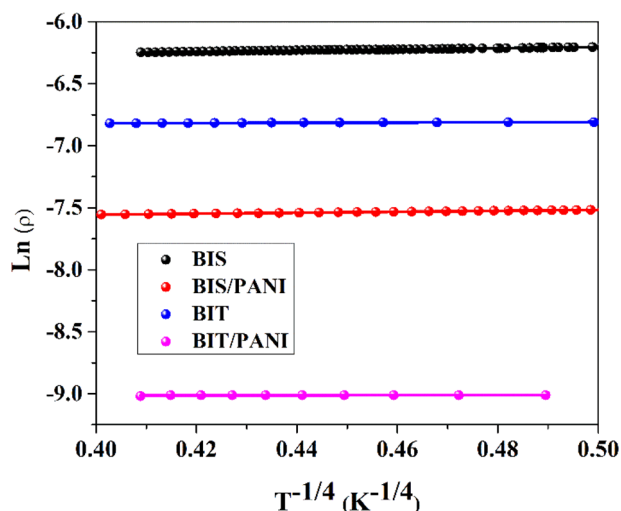


Fig. 9 Linear fitting of SPH model in the high temperature region for BIT/PANI and BIS/PANI composites

which results from the exchange of energy between electrons and the lattice, is generated by the adsorption of polarons at disordered sites [28].

Electrons hop between the closest localized sites between inverse of temperature 30 and 130 K (Fig. 10). The primary mechanism of conduction below 130 K is electron hopping, which occurs in a constrained energy band around the chemical potential [29, 30]. Electrons are concentrated at this potential level due to their electronic states and jumps to the closest localised state. The thermal energy of the electrons regulates conductivity. Internal atomic disorder due to doping

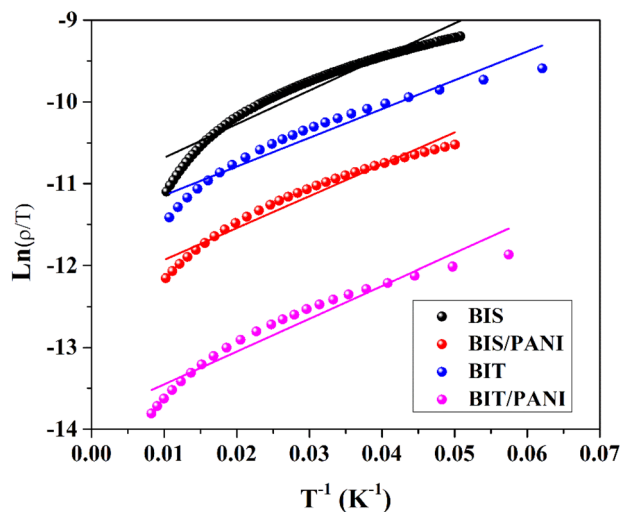


Fig. 10 Variation of $\ln(\rho/T)$ versus T^{-1} for BIT/PANI and BIS/PANI composites (VRH Plot)

causes tunnelling between nearest places, limiting conductivity in VRH. At temperatures below 130 K, electrons gain energy and hop to closer states. The thermal energy of electrons sets a limit on conductivity. At low temperatures, probability of thermal activation of electron decreases with decreasing energy, but the probability of hopping between distant states increases. As temperature drops, the average hopping distance of electron increases [31]. The typical temperature (T_0) and pre-exponential factor (ρ_0) are calculated using the slope, and are depicted in Table 2.

3.4 Seebeck coefficient

Figure 11 represents the temperature-dependent Seebeck coefficient in the range 10–350 K. According to observations, each compound exhibits *n*-type nature in which electrons predominate as charge carriers [32]. The Seebeck coefficient found to increase with increase in temperature. The crystal flaw that brings the conduction band closer to the donor band is the reason for the increased Seebeck coefficient. The presence of nitro group of PANI with numerous grain boundaries contributing significantly for the surface roughness and is responsible for the fluctuation in the Seebeck coefficient with varying percentages of PANI in BIT and BIS [33, 34]. According to literature, elements like tellurium and selenium exhibit high carrier dispersion and charge carrier effects, which also contributes to enhance Seebeck coefficient value. These results are

Table 2 Experimental (n_{Exp}), theoretical carrier concentration (n_{Th}); experimental (m_{Exp}), Theoretical (m_{Th}) carrier mobility; experimental (γ_{Exp}); Fermi energy (E_F), activation energy (E_A), pre-exponential factor (ρ_0), characteristic temperature (T_0) of BIT/PANI and BIS/PANI composites

Sample	n_{Th} (m^{-3})	m_{Exp} $10^{-4}(m^2/Vs)$	γ_{Exp}	E_A (meV)	E_F (eV)	ρ_0 10^{-5} (W m)	T_0 10^{-3} (K)
$(Bi_{0.98}In_{0.02})_2Te_{2.7}Se_{0.3}$	7.87×10^{19}	1.2	45.8	3.5	72	15	1.22
$(Bi_{0.98}In_{0.02})_2Te_{2.7}Se_{0.3}/0.02wt\%$ Polyaniline	1.16×10^{20}	2825	34.5	3.2	12	6.0	1.26
$(Bi_{0.98}In_{0.02})_2Se_{2.7}Te_{0.3}$	1.14×10^{19}	0.935	46.1	3.0	73	11	1.77
$(Bi_{0.98}In_{0.02})_2Se_{2.7}Te_{0.3}/0.02wt\%$ Polyaniline	8.03×10^{15}	38.92	38.9	3.4	52	9	2.18''

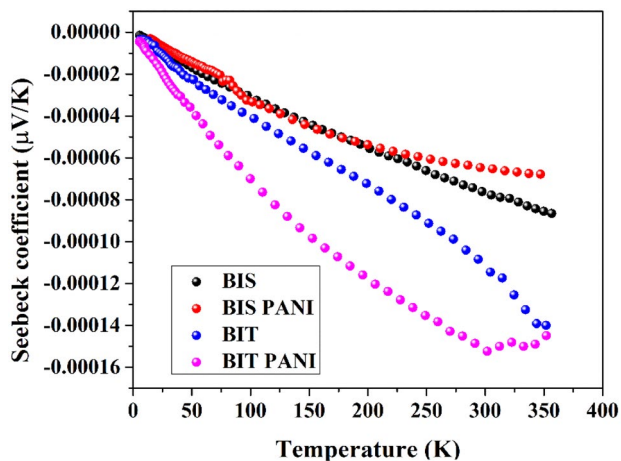


Fig. 11 Temperature-dependent Seebeck coefficient of BIT/PANI and BIS/PANI composites

typically observed in materials with bulk surfaces, owing to the weight that the FESEM images support [35].

The correlation between transport characteristics and Hall effect findings shows n -type nature of all the samples, serves as proof for the Seebeck coefficient. It has been observed that there is a significant dispersion in the grain boundaries because of the increased grain size, having an impact on the variance of the microstructure in the surface. By using $\gamma = \ln(n) + S$ the scattering factor has been computed, n denoting the carrier concentration and S is the Seebeck coefficient [36]. Table 2 provides the scattering factor for each sample.

3.5 Thermal conductivity

Figure 12 depicts how the samples' thermal conductivity varies with temperature. Due to greater Umklapp dispersion, the total thermal conductivity of the composite samples is lower than that of BIT

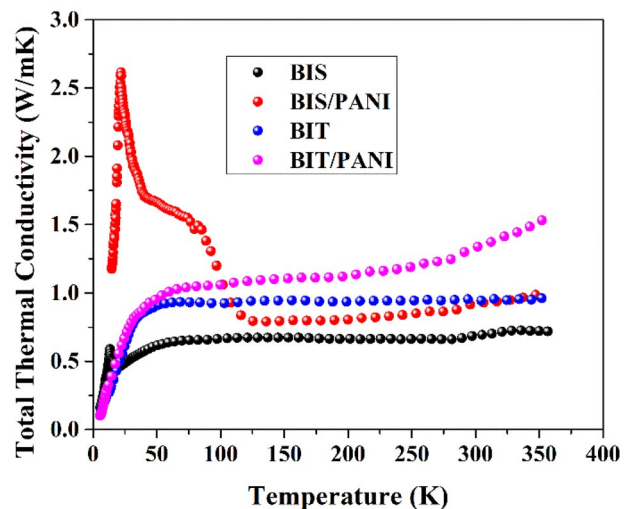


Fig. 12 Total thermal conductivity of BIT/PANI and BIS/PANI composites

above 50 K [37]. The limited interface charge dispersion that results from the accumulation of PANI on BIT and BIS is what causes the thermal conductivity's uniform ordering characteristic. Therefore, the interface scattering effect of PANI composites, and the BIT/BIS grain boundaries have a strong influence on the decrease in total thermal conductivity [38]. The Umklapp process dominates resistivity at higher temperatures, and crystal relaxation reduces the mean free path of phonons. Due to defects or boundary scattering of BIT/PANI and BIS/PANI interfaces in the crystals, the mean free path for well-ordered materials lengthens with decreasing temperature until it hits its limit [39]. The Wiedemann-Franz law links the electronic (Fig. 13) and lattice components, which make up the overall thermal conductivity. ($\kappa_e = \frac{L_0 T}{\rho}$) where L_0 is the Lorentz number ($2.50 \times 10^{-8} \text{ W}\Omega\text{K}^{-2}$) calculated using

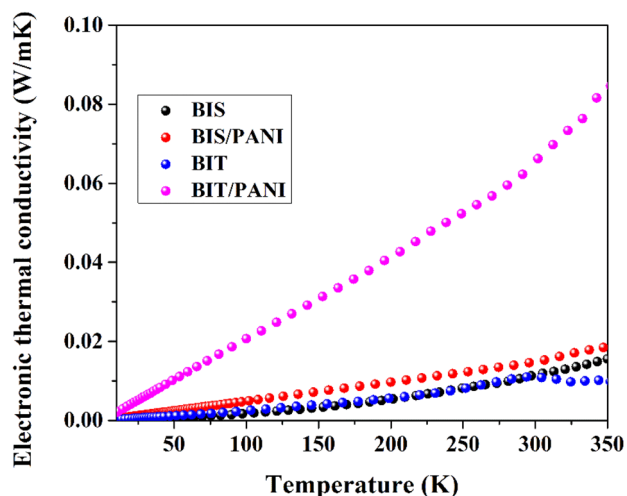


Fig. 13 Electronic thermal conductivity of BIT/PANI and BIS/PANI composites

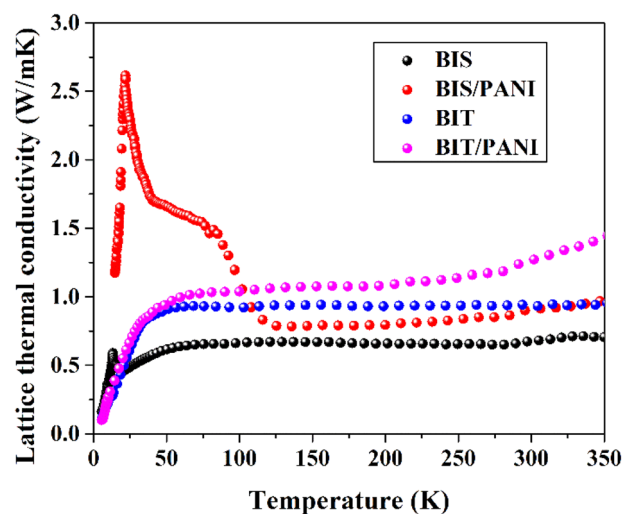


Fig. 15 Lattice thermal conductivity of BIT/PANI and BIS/PANI composites

$$L_0 = 1.5 + \exp\left[-\left(\frac{|S|}{116}\right)\right]$$

Figure 14 displays the temperature-dependent Lorentz number. By deducting the electronic thermal conductivity from the total thermal conductivity (K_t), the lattice component of the thermal conductivity (K_e) [Fig. 15] is obtained. To lower the binary Schottky barrier, PANI is poured into the grain boundaries. The uncovered grains serve as scattering locations for carrier mobility and antisite defect scattering since some BIS/BIT's microstructure has an uneven distribution of grains. Scattering centres have little effect on the speed of phonons in solids, while they have little effect on the specific heat of the solids. Hence impurities have

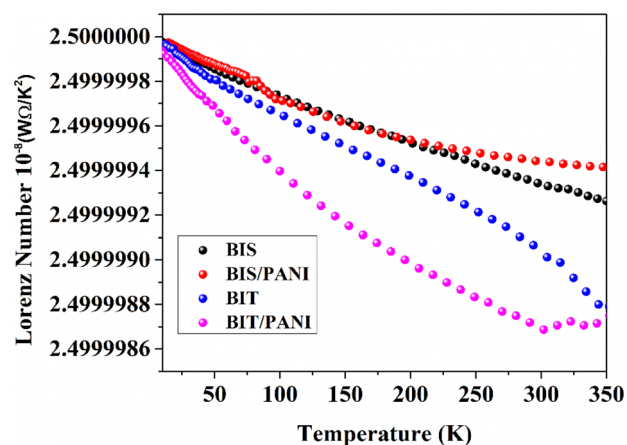


Fig. 14 Lorentz Number of BIT/PANI and BIS/PANI composites

the largest effect at the low temperature. The phonons are limited by the interface boundaries formed between the BIS/PANI and BIT/PANI [40]. According to the reported results, K_l can be reduced by selective scattering of phonons by conducting polymers such as PANI inclusions in the crystal which scatters phonons more than electrons, depending on their respective scattering length. The similar results have been shown in our previous research work also. Along with these outcomes, the replacement is likely responsible for the mass and size contrast, which leads to lattice point defects in the crystal [41, 42]. As a result, at low temperatures, the grain boundary scattering caused by PANI and the point defect scattering caused by dopants like indium and selenium/tellurium have a considerable impact on the thermal transport property. Atomic flaws like vacancies and antisite disorder may also have an impact on thermal conductivity because they cause phonons that carry heat to travel at a shorter average wavelength [43].

3.6 Thermo power and thermoelectric figure of merit

Figures 16 and 17 represent the calculated and observed temperature-dependent power factor (PF) and TE figure of merit (ZT) values of PANI, BIT, BIS and their composites, respectively. The sample doped with BIT/PANI shows the maximum PF of 0.00023 $\mu\text{W}/\text{mK}^2$ and ZT value of 0.045 at 350 K.

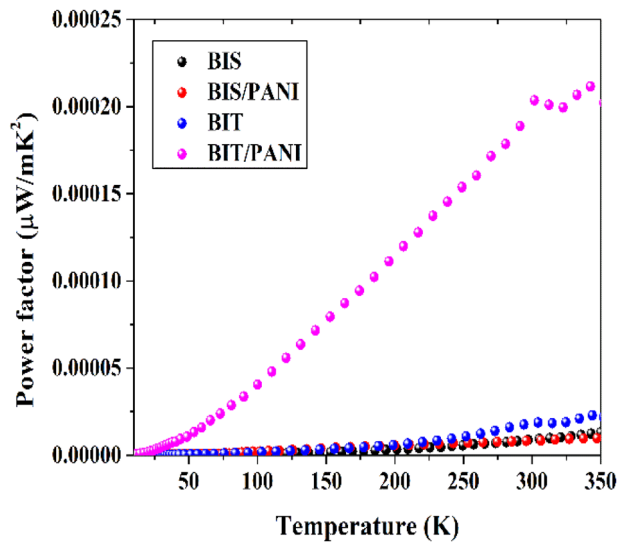


Fig. 16 Thermoelectric Power factor of BIT/PANI and BIS/PANI composites

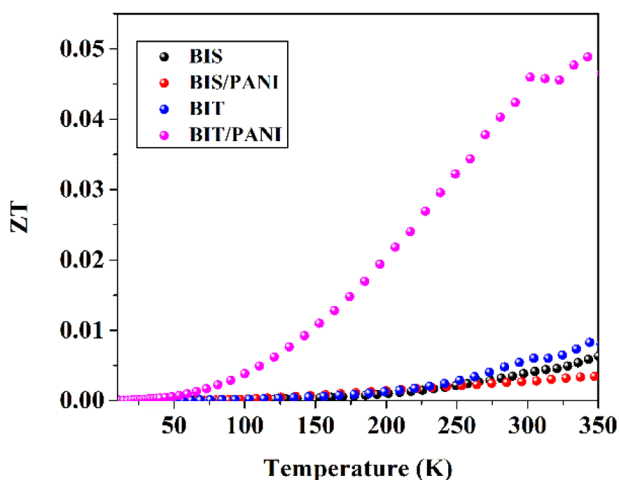


Fig. 17 Thermoelectric figure of merit of BIT/PANI and BIS/PANI composites

Sample BIS/PANI, in contrast, exhibits the lowest PF and ZT values ($0.4 \mu\text{W}/\text{mK}^2$ and 0.005). At low temperatures, the grain boundary scattering caused by PANI and the point defect scattering caused by dopants like indium and selenium/tellurium have a considerable impact on the thermal transport property. Atomic flaws like vacancies and antisite disorder may also have an impact on thermal conductivity due to a drop in the average wavelength of heat-carrying phonons. Hence, there is a variation in electrical resistivity, Seebeck coefficient and thermal

conductivity between the synthesized compounds may be the reason for their lower ZT.

4 Conclusions

In this work, the TE performance of composites made of $(\text{Bi}_{0.98}\text{In}_{0.02})_2\text{Te}_{2.7}\text{Se}_{0.3}$ / Polyaniline and $(\text{Bi}_{0.98}\text{In}_{0.02})_2\text{Se}_{2.7}\text{Te}_{0.3}$ /Polyaniline composites in the low temperature range of 10 to 350 K was examined. The XRD analysis reveals that the crystal structure is hexagonal with an $R\bar{3}m$ space group. The electrical resistivity in the BIS/PANI sample has dropped six times when compared to the BIT/PANI sample. The reduction in overall thermal conductivity has been strongly influenced by the BIT/BIS grain boundaries and the interface scattering effect of PANI composites. In comparison to BIT/PANI and BIS/PANI, the thermal conductivity of pure BIT is reduced by 1.5 and 1.4 times, respectively. The ZT value of BIT/PANI is found to increase by 20 times compared to pure BIT samples. Hence, BIT/PANI could be a potential candidate for the low-temperature TE applications.

Acknowledgements

“Ganesh Shridhar Hegde (GSH) acknowledges Manipal Academy of Higher Education for supporting him financially through the Dr. T. M. A. doctorate fellowship. Thank you to UDCSR/MUM/AO/CRS-M-314/2022/12 for providing the physical property measuring system, on behalf of one of the authors (ANP). The authors would like to thank Dr. Shabana Bano for providing the FESEM facility from UGC DAE Kalpakam, Tamilnadu.”

Author contributions

Conception: MYB. Experimental design: GSH. Carrying out measurements: PDB, SP. Manuscript composition: ANP.

Funding

Open access funding provided by Manipal Academy of Higher Education, Manipal. This work was supported by UGC-DAE Consortium for Scientific

Research, University Grants Commission (Grant No: UDCSR/MUM/AO/CRS-M-314/2022/12).

Data availability

The thermoelectric data were generated at UGC DAE CSR Mumbai. The findings of this study are available from the corresponding author [ANP] on request. The datasets generated during and/or analysed during the current study are available from the corresponding author on reasonable request

Declarations

Conflict of interest All authors certify that they have no affiliations with or involvement in any organization or entity with any financial interest or non-financial interest in the subject matter or materials discussed in this manuscript.”

Ethical approval The research leading to these results received funding from project grant UDCSR/MUM/AO/CRS-M-314/2022/12. We ensure that all research is conducted in accordance with ethical principles.

Open Access This article is licensed under a Creative Commons Attribution 4.0 International License, which permits use, sharing, adaptation, distribution and reproduction in any medium or format, as long as you give appropriate credit to the original author(s) and the source, provide a link to the Creative Commons licence, and indicate if changes were made. The images or other third party material in this article are included in the article's Creative Commons licence, unless indicated otherwise in a credit line to the material. If material is not included in the article's Creative Commons licence and your intended use is not permitted by statutory regulation or exceeds the permitted use, you will need to obtain permission directly from the copyright holder. To view a copy of this licence, visit <http://creativecommons.org/licenses/by/4.0/>.

References

1. B.S. Nagaraja, A. Rao, P.D. Babu, G.S. Okram, *Phys. B Phys. Condens. Matter.* **479**, 10 (2015)
2. X.A. Fan, J.Y. Yang, W. Zhu, H.S. Yun, R.G. Chen, S.Q. Bao, X.K. Duan, *J. Alloys Compd.* **420**, 256 (2006)
3. S. Schreyeck, N.V. Tarakina, G. Karczewski, C. Schumacher, T. Borzenko, C. Brüne, H. Buhmann, C. Gould, K. Brunner, L.W. Molenkamp, *Appl. Phys. Lett.* **102**, 041914 (2013)
4. P.F.P. Poudeu, J. D'Angelo, H. Kong, A. Downey, J.L. Short, R. Pcionek, T.P. Hogan, C. Uher, M.G. Kanatzidis, *J. Am. Chem. Soc.* **128**, 14347 (2006)
5. U.S. Shenoy, D.K. Bhat, *J. Mater. Chem. C* **7**, 4817 (2019)
6. G. Ding, G. Gao, K. Yao, *Sci. Rep.* **5**, 1 (2015)
7. W. Li, R. Zamani, P. Rivera Gil, B. Pelaz, M. Ibáñez, D. Cadavid, A. Shavel, R.A. Alvarez-Puebla, W.J. Parak, J. Arbiol, A. Cabot, *J. Am. Chem. Soc.* **135**, 7098 (2013)
8. W.-S. Liu, Q. Zhang, Y. Lan, S. Chen, X. Yan, Q. Zhang, H. Wang, D. Wang, G. Chen, Z. Ren, *Adv. Energy Mater.* **1**, 577 (2011)
9. M. Ohta, K. Biswas, S.-H. Lo, J. He, D.Y. Chung, V.P. Dravid, M.G. Kanatzidis, *Adv. Energy Mater.* **2**, 1117 (2012)
10. J.-H. Bahk, H. Fang, K. Yazawa, A. Shakouri, *J. Mater. Chem. C* **3**, 10362 (2015)
11. R. Nayak, P. Shetty, S.M.A. Rao, K.M. Rao, *Energy.* **238**, 121680 (2022)
12. C. Guo, F. Chu, P. Chen, J. Zhu, H. Wang, L. Wang, Y. Fan, W. Jiang, *J. Mater. Sci.* **53**, 6752 (2018)
13. M. Diantoro, I.N. Fitriana, F. Parasmayanti, A. Nasikhudin, N. Taufiq, Sunaryono, Mufti, H. Nur, *IOP Conf. Ser. Mater. Sci. Eng.* **202**, (2017)
14. M. Noroozi, G. Jayakumar, K. Zahmatkesh., J. Lu, L. Hultman, M. Mensi, S. Marcinkevicius, B. Hamawandi, M.Y. Tafti, A.B. Ergül, Z. Ikonic, *ECS J. Solid State Sci. Technol.* **6**, Q114 (2017)
15. Y. Li, G. Wang, M. Akbari-Saatlu, M. Procek, H. Radamson, *Sec. Energy Mater.* (2021). <https://doi.org/10.3389/fmats.2021.611078>
16. G.S. Hegde, V. Parol, A. Rao, A.N. Prabhu, J.J.B. Levinsky, G.R. Blake, *Mater. Res. Bull.* **145**, 111517 (2022)
17. Y. Li, Q. Zhao, Y.G. Wang, K. Bi, *Mater. Sci. Semicond. Process.* **14**, 219 (2011)
18. S. Subramanian, D.P. Padiyan, *Mater. Chem. Phys.* **107**, 392 (2008)
19. K. Chatterjee, A. Suresh, S. Ganguly, K. Kargupta, D. Banerjee, *Mater. Charact.* **60**, 1597 (2009)
20. G.S. Hegde, A.N. Prabhu, A. Rao, P.D. Babu, *Phys. B Condens. Matter.* **584**, 412087 (2020)

21. M.S. Shalaby, E.O. Taha, S. Abdelhaleem, J. Alloys Compd. **920**, 165975 (2022)
22. H.J. Wu, B.Y. Chen, H.Y. Cheng, Acta Mater. **122**, 120 (2017)
23. M.S. Shalaby, S. Abdelhaleem, A. Sotelo, Synth. Met. **285**, 117025 (2022)
24. F. Li, M. Ruan, Y. Chen, W. Wang, J. Luo, Z. Zheng, P. Fan, Inorg. Chem. Front. **6**, 799 (2019)
25. R.R. Urkude, P.T. Patil, S.B. Kondawar, U.A. Palikundwar, Procedia Mater. Sci. **10**, 205 (2015)
26. J.U. Rahman, N. Van Du, W.H. Nam, W.H. Shin, K.H. Lee, W.S. Seo, M.H. Kim, S. Lee, Sci. Rep. **9**, 1 (2019)
27. J. Andzane, K. Buks, M.N. Strakova, M. Zubkins, M. Bechelany, M. Marnauza, M. Baitimirova, D. Erts, IEEE Trans. Nanotechnol. **18**, 948 (2019)
28. M. Rudra, R.A. Kumar, H.S. Tripathi, R. Sutradhar, T.P. Sinha, 9033, 0 (n.d.).
29. J.H. Kim, Y.J. Song, J.S. Rhyee, B.S. Kim, S.D. Park, H.J. Lee, J.W. Shin, Phys. Rev. B - Condens. Matter Mater. Phys. **87**, 1 (2013)
30. A. Banerjee, S. Pal, E. Rozenberg, B.K. Chaudhuri, J. Phys. Condens. Matter. **13**, 9489 (2001)
31. O. Ivanov, M. Yaprntsev, E. Danshina, Phys. B: Condens. Matter. **545**, 222–227 (2018)
32. G.S. Hegde, A.N. Prabhu, Y.H. Gao, Y.K. Kuo, V.R. Reddy, J. Alloys Compd. **866**, 158814 (2021)
33. F.T. Johra, J.W. Lee, W.G. Jung, J. Ind. Eng. Chem. **20**, 2883 (2014)
34. M. Mitra, K. Kargupta, S. Ganguly, S. Goswami, D. Banerjee, Synth. Met. **228**, 25 (2017)
35. H. Chen, C. Yang, H. Liu, G. Zhang, D. Wan, F. Huang, CrystEngComm. **15**, 6648 (2013)
36. A.M. Adam, A. Elshafaie, A.E.-M.A. Mohamed, P. Petkov, E.M.M. Ibrahim, Mater. Res. Express. **5**, 035514 (2018)
37. I. Terasaki, in Ref. Modul. Mater. Sci. Mater. Eng (Elsevier, 2016), pp. 1–40
38. M. Mitra, C. Kulsi, K. Kargupta, S. Ganguly, D. Banerjee, J. Appl. Polym. Sci. **135**, 46887 (2018)
39. K. Chatterjee, M. Mitra, K. Kargupta, S. Ganguly, D. Banerjee, Nanotechnology. **24**, 215703 (2013)
40. S. Paul, U. Pal, S.K. Pradhan, J. Alloys Compd. **858**, 157732 (2021)
41. H. Ju, J. Kim, J. Alloys Compd. **664**, 639 (2016)
42. G. Sun, X. Qin, D. Li, J. Zhang, B. Ren, T. Zou, H. Xin, S.B. Paschen, X. Yan, J. Alloys Compd. **639**, 9 (2015)
43. G.S. Hegde, A.N. Prabhu, R.Y. Huang, Y.K. Kuo, J. Mater. Sci. Mater. Electron. **31**, 19511 (2020)

Publisher's note Springer Nature remains neutral with regard to jurisdictional claims in published maps and institutional affiliations.